Subpixel displacement and deformation gradient measurement using digital image/speckle correlation (DISC)

Peng Zhou
Kenneth E. Goodson
Stanford University
Mechanical Engineering Department
Stanford, California 94305-3030
E-mail: goodson@vk.stanford.edu

Abstract. Experimental solid mechanics relies heavily on surface displacement and deformation gradient measurements. Digital image/speckle correlation (DISC) uses digital image processing to resolve displacement and deformation gradient fields. The practical implementation of DISC involves important challenges such as computation complexity and the discrepancy of the sensitivities and accuracies claimed in previous studies. We develop an iterative, spatial-gradient based algorithm, which uses only first-order spatial derivatives of the images before and after deformation. Simulated images are then used to verify this algorithm, as well as to study the impact of speckle size on the accuracy. Based on these simulations, the sensitivity of DISC to displacement and deformation gradient, as well as an optimal speckle size for optimal accuracy, is recommended. The algorithm is then calibrated using rigid body translation and rotation, and an application of DISC to thermomechanical diagnostics of electronic packaging is also presented. [DOI: 10.1117/1.1387992]

Subject terms: digital image/speckle correlation; cross correlation; subpixel deformation; image processing.

Paper 200141 received Apr. 6, 2000; revised manuscript received Oct. 17, 2000; accepted for publication Feb. 21, 2001.

1 Introduction

Recently, a variety of optical metrology techniques have been developed to measure noncontact, full-field displacement and deformation gradient distributions in experimental solid mechanics. These include both interferometric techniques, such as holographic interferometry, speckle interferometry and moiré interferometry, and noninterferometric ones, such as speckle photography and moiré. Interferometric techniques rely on the detection of the optical phase difference on the specimen surface before and after deformation. This phase difference yields a fringe pattern, which often represents the contour lines of the surface displacement. Noninterferometric techniques directly compare the optical intensity pattern on the deformed specimen surface, which is often called the specimen pattern, with another reference pattern. For moiré, the specimen pattern is a distorted specimen grating, and the reference pattern is an undistorted reference grating. However, these patterns do not have to be periodical lines or grids. For example, in speckle photography, the specimen pattern is the speckle pattern after deformation, while the reference pattern is just the speckle pattern before deformation.

Digital image processing is becoming more important for optical metrology, because the introduction of electronic imaging devices, such as charge-coupled devices (CCD), eliminates the necessity of wet photographic process. The applications of digital image processing in interferometric techniques include various phase-shifting/phase stepping algorithms, which greatly enhance the efficiencies and accuracies of these techniques by directly calculating the optical phase instead of tedious fringe analysis. Digital image processing is also used in noninterferometric techniques, such as computer aided speckle interferometry (CASI), which simulates the optical filtering process of conventional speckle photography through the use of fast Fourier transform (FFT) in pointwise Young's fringe analysis and full-field displacement fringe analysis.[1]

Digital image/speckle correlation (DISC) also uses digital image processing to resolve displacement and deformation gradient fields.[2] The underlying principle of DISC is rather simple: the tracking of a geometric point before and after deformation yields its displacement vector. While this technique is simple in principle, the practical implementation offers important challenges. One of the challenges is the computation complexity. Because of the discrete nature of digital images, most of the existing algorithms require data interpolation or fitting, which is computationally complex. In addition, iterative algorithms often require the calculation of second-order spatial derivatives of the digital images, which further increases computation complexity. Moreover, the sensitivities and accuracies claimed in various previous studies vary within orders of magnitude from 0.5 pixel (Ref. 3) to 0.01 pixel (Ref. 4). However, few quantitative works have been performed to resolve this discrepancy.

In this paper, an iterative, spatial-gradient based algorithm is developed that requires the calculation of only first-order spatial derivatives of the images and thus reduces computation complexity. Simulated images are then used to verify this algorithm as well as to study the impact

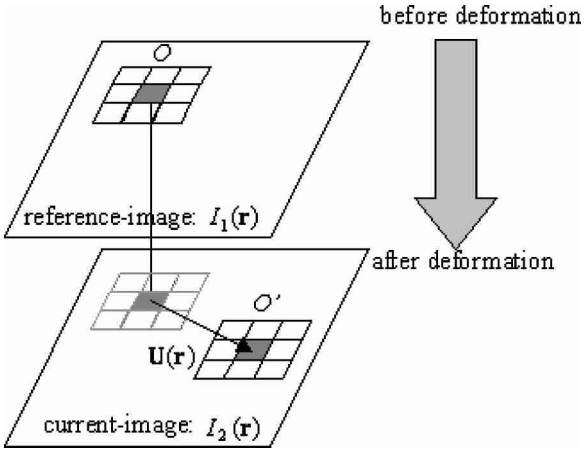

Fig. 1 Schematic showing the principle of DISC. The images of the sample before and after deformation are called the reference image $I_1(\mathbf{r})$ and the current image $I_2(\mathbf{r})$, respectively. A reference pixel O in the reference image experiences a deformation of $\mathbf{U}(\mathbf{r})$ to the current pixel position O'.

of speckle size on the accuracy. Based on these simulations, an optimal speckle size is also recommended. The algorithm is then calibrated under rigid body translation and rotation, and an application of DISC to thermomechanical diagnostics of electronic packaging is also presented.

2 DISC

2.1 *Principles*

DISC was first developed[2] to measure displacements in experimental solid mechanics. Given the time interval between two digital images, the velocity fields of fluids can also be determined, which is the basis of particle image velocimetry (PIV) in experimental fluid mechanics (e.g., Ref. 5). DISC can also be applied with computer vision theory or laser holography theory to measure 3-D displacement or velocity fields.[6,7]

The underlying principle of DISC is that the tracking of a geometric point before and after deformation yields its displacement. In practice, this tracking is achieved through the image processing of speckle patterns on the specimen surface. Laser speckle is the random interference pattern generated by a rough surface under coherent illumination. In general, however, any random intensity distribution can also be considered as a speckle pattern.[8] For example, an artificial speckle pattern can be generated by spraying white paint onto a black substrate.

As shown in Fig. 1, speckle patterns on the specimen surface before and after deformation are captured and digitized into two digital images. These two images are called the reference image $I_1(\mathbf{r})$ and the current image $I_2(\mathbf{r})$, which are related as follows:

$$I_2(\mathbf{r}) = I_1[\mathbf{r} - \mathbf{U}(\mathbf{r})], \tag{1}$$

$$I_1(\mathbf{r}) = I_2[\mathbf{r} + \mathbf{U}(\mathbf{r})], \tag{2}$$

where $\mathbf{U}(\mathbf{r})$ is the displacement vector at pixel $\mathbf{r} = (x,y)^T$. A subimage around a reference pixel O in the reference image is then compared with subimages corresponding to different pixels in the current image using a predefined correlation function to describe the difference of two digital subimages. Three typical correlation functions are defined as follows:

absolute difference:

$$C_A(\mathbf{r}') = 1 - \frac{\int\int_\Omega |I_2(\mathbf{r}+\mathbf{r}') - I_1(\mathbf{r})|\, d\mathbf{r}}{\int\int_\Omega I_1(\mathbf{r})\, d\mathbf{r}}, \tag{3}$$

least square:

$$C_L(\mathbf{r}') = 1 - \frac{\int\int_\Omega [I_2(\mathbf{r}+\mathbf{r}') - I_1(\mathbf{r})]^2 d\mathbf{r}}{\int\int_\Omega I_1^2(\mathbf{r})\, d\mathbf{r}}, \tag{4}$$

and cross-correlation:

$$C_C(\mathbf{r}') = \frac{\int\int_\Omega I_1(\mathbf{r}) I_2(\mathbf{r}+\mathbf{r}')\, d\mathbf{r}}{[\int\int_\Omega I_1^2(\mathbf{r})\, d\mathbf{r} \int\int_\Omega I_2^2(\mathbf{r}+\mathbf{r}')\, d\mathbf{r}]^{1/2}} \tag{5}$$

where Ω $(M \times N)$ is the area of the subimage around pixel $\mathbf{r}$. In practice, the absolute difference and least squares correlation functions require less computation, while the normalized cross-correlation function is more computationally demanding. Based on these correlation functions, a certain pixel in the current-image where two subimages reach best matching and thus maximize the correlation function is called the current-pixel O'. The difference of the positions of the current pixel (O') and the reference pixel (O) yields the in-plane displacement $\mathbf{U}(\mathbf{r})$ of this reference pixel. The full-field in-plane displacement can thus be obtained by changing the reference pixel and repeating the just-described process.

2.2 *Subpixel Displacement Estimation*

The displacement calculated from Section 2.1 is an integral multiple of one pixel dimension due to the discrete aspect of digital images. Subpixel algorithms are required to further enhance the sensitivity and accuracy of the measurement. The algorithm used for subpixel displacement estimation is an optical flow method developed by Davis and Freeman.[9]

To estimate subpixel displacements $\mathbf{U}(\mathbf{r})$ in a subimage corresponding to a pixel $\mathbf{r}_0 = (x_0, y_0)^T$ in the current image $I_2(\mathbf{r})$ is assumed be a constant:

$$\mathbf{U}(\mathbf{r}) = \mathbf{U}(\mathbf{r}_0) = \mathbf{U}_0 = (u_0, v_0)^T. \tag{6}$$

Equations (1) and (2) can then be rewritten as

$$I_2(\mathbf{r}) = I_1(\mathbf{r} - \mathbf{U}_0), \tag{7}$$

$$I_1(\mathbf{r}) = I_2(\mathbf{r} + \mathbf{U}_0). \tag{8}$$

After neglecting high order terms, Taylor expansion of these two equations yields:

$$I_2(\mathbf{r}) = I_1(\mathbf{r}) - \nabla I_1(\mathbf{r}) \cdot \mathbf{U}_0, \tag{9}$$

$$I_1(\mathbf{r}) = I_2(\mathbf{r}) + \nabla I_2(\mathbf{r}) \cdot \mathbf{U}_0, \tag{10}$$

where $\nabla I_1(\mathbf{r})$ and $\nabla I_2(\mathbf{r})$ are spatial gradients of two images. Equations (9) and (10) can be rearranged as:

$$[\nabla I_1(\mathbf{r}) + \nabla I_2(\mathbf{r})] \cdot \mathbf{U}_0 = 2[I_1(\mathbf{r}) - I_2(\mathbf{r})]. \tag{11}$$

Equation (11) holds for $M \times N$ pixels in a subimage Ω around $\mathbf{r}_0$ and therefore leads to $M \times N$ equations. The least squares approximate solution to these equations is then determined by:

$$\mathbf{A}^T\mathbf{A} \cdot \mathbf{U}_0 = \mathbf{A}^T \cdot \mathbf{b}, \tag{12}$$

where

$$\mathbf{A} = \begin{pmatrix} \cdot \\ \cdot \\ \nabla^T I_1(\mathbf{r}) + \nabla^T I_2(\mathbf{r}) \\ \cdot \\ \cdot \end{pmatrix}_{M \cdot N \times 2, \mathbf{r} \in \Omega} \tag{13}$$

$$\mathbf{b} = \begin{pmatrix} \cdot \\ \cdot \\ 2[I_1(\mathbf{r}) - I_2(\mathbf{r})] \\ \cdot \\ \cdot \end{pmatrix}_{M \cdot N \times 1, \mathbf{r} \in \Omega} \tag{14}$$

2.3 *Subpixel Displacement and Deformation Gradient Calculation Using Newton's Iteration*

To further determine subpixel displacement and deformation gradients, $\mathbf{U}(\mathbf{r})$ in a subimage corresponding to a pixel $\mathbf{r}_0$ in the current image $I_2(\mathbf{r})$ is assumed to be a linear function with respect to $\mathbf{r}$, with a displacement of $\mathbf{U}_0 = (u_0, v_0)^T$ at $\mathbf{r}_0$, and a constant deformation gradient

$$\nabla \mathbf{U}_0 = \begin{pmatrix} u_x & u_y \\ v_x & v_y \end{pmatrix}:$$

$$\mathbf{U}(\mathbf{r}) = \mathbf{U}_0 + \nabla \mathbf{U}_0(\mathbf{r} - \mathbf{r}_0). \tag{15}$$

Based on Eq. (15), Eqs. (1) and (2) can be rewritten as:

$$I_2(\mathbf{r}) = I_1[\mathbf{r} - \mathbf{U}_0 - \nabla \mathbf{U}_0(\mathbf{r} - \mathbf{r}_0)] \tag{16}$$

$$I_1(\mathbf{r}) = I_2[\mathbf{r} + \mathbf{U}_0 + \nabla \mathbf{U}_0(\mathbf{r} - \mathbf{r}_0)]. \tag{17}$$

Newton's iteration scheme can then be applied to these two equations, yielding:

$$\nabla I_1[\mathbf{r} - \mathbf{U}_0^k - \nabla \mathbf{U}_0^k(\mathbf{r} - \mathbf{r}_0)] \cdot [\delta \mathbf{U}_0^k + \delta \nabla \mathbf{U}_0^k(\mathbf{r} - \mathbf{r}_0)] = R_1^k(\mathbf{r}, \mathbf{U}_0^k, \nabla \mathbf{U}_0^k), \tag{18}$$

$$\nabla I_2[\mathbf{r} + \mathbf{U}_0^k + \nabla \mathbf{U}_0^k(\mathbf{r} - \mathbf{r}_0)] \cdot [\delta \mathbf{U}_0^k + \delta \nabla \mathbf{U}_0^k(\mathbf{r} - \mathbf{r}_0)] = -R_2^k(\mathbf{r}, \mathbf{U}_0^k, \nabla \mathbf{U}_0^k) \tag{19}$$

where

$$R_1^k(\mathbf{r}, \mathbf{U}_0^k, \nabla \mathbf{U}_0^k) = I_1[\mathbf{r} - \mathbf{U}_0^k - \nabla \mathbf{U}_0^k(\mathbf{r} - \mathbf{r}_0)] - I_2(\mathbf{r}), \tag{20}$$

$$R_2^k(\mathbf{r}, \mathbf{U}_0^k, \nabla \mathbf{U}_0^k) = I_2[\mathbf{r} + \mathbf{U}_0^k + \nabla \mathbf{U}_0^k(\mathbf{r} - \mathbf{r}_0)] - I_1(\mathbf{r}), \tag{21}$$

where $\mathbf{U}_0^k$ and $\nabla \mathbf{U}_0^k$ are the displacement vector and the deformation gradient tensor at $\mathbf{r}_0$ for the k'th round iteration; $\delta \mathbf{U}_0^k$ and $\delta \nabla \mathbf{U}_0^k$ are the increments of the displacement vector and the deformation gradient tensor at $\mathbf{r}_0$ for the k'th round iteration, which are related as follows:

$$\mathbf{U}_0^{k+1} = \mathbf{U}_0^k + \delta \mathbf{U}_0^k, \tag{22}$$

$$\nabla \mathbf{U}_0^{k+1} = \mathbf{U}_0^k + \delta \nabla \mathbf{U}_0^k. \tag{23}$$

A new equation can be obtained by combing Eqs. (18) and (19)

$$\{\nabla I_1[\mathbf{r} - \mathbf{U}_0^k - \nabla \mathbf{U}_0^k(\mathbf{r} - \mathbf{r}_0)] + \nabla I_2[\mathbf{r} + \mathbf{U}_0^k + \nabla \mathbf{U}_0^k(\mathbf{r} - \mathbf{r}_0)]\} \cdot [\delta \mathbf{U}_0^k + \delta \nabla \mathbf{U}_0^k(\mathbf{r} - \mathbf{r}_0)] = R_1^k(\mathbf{r}, \mathbf{U}_0^k, \nabla \mathbf{U}_0^k) - R_2^k(\mathbf{r}, \mathbf{U}_0^k, \nabla \mathbf{U}_0^k). \tag{24}$$

Again, this equation holds for $M \times N$ pixels in a subimage around $\mathbf{r}_0$ and therefore leads to $M \times N$ equations. The least squares approximate solution to these equations is determined by:

$$(\mathbf{C}^k)^T \mathbf{C}^k \delta \mathbf{P}^k = (\mathbf{C}^k)^T \mathbf{d}^k, \tag{25}$$

where

$$\mathbf{C}^k = \begin{pmatrix} \cdot & & & & & \\ \cdot & & & & & \\ c_1^k & c_2^k & c_3^k & c_4^k & c_5^k & c_6^k \\ \cdot & & & & & \\ \cdot & & & & & \end{pmatrix}_{M \cdot N \times 6, \mathbf{r} \in \Omega}, \tag{26}$$

$$\mathbf{d}^k = (R_1^k(\mathbf{r}, \mathbf{U}_0^k, \nabla \mathbf{U}_0^k) - R_2^k(\mathbf{r}, \mathbf{U}_0^k, \nabla \mathbf{U}_0^k))_{M \cdot N \times 1, \mathbf{r} \in \Omega}, \tag{27}$$

$$c_1^k = \frac{\partial I_1(\mathbf{r} - \mathbf{U}_0^k - \nabla \mathbf{U}_0^k(\mathbf{r} - \mathbf{r}_0)}{\partial x} + \frac{\partial I_2[\mathbf{r} + \mathbf{U}_0^k + \nabla \mathbf{U}_0^k(\mathbf{r} - \mathbf{r}_0)]}{\partial x}, \tag{28}$$

$$c_2^k = (x - x_0)c_1^k, \tag{29}$$

$$c_3^k = (y - y_0)c_1^k, \tag{30}$$

$$c_4^k=\frac{\partial I_1(\mathbf{r}-\mathbf{U}_0^k-\nabla\mathbf{U}_0^k(\mathbf{r}-\mathbf{r}_0)}{\partial y}+\frac{\partial I_2(\mathbf{r}+\mathbf{U}_0^k+\nabla\mathbf{U}_0^k(\mathbf{r}-\mathbf{r}_0)]}{\partial y}, \tag{31}$$

$$c_5^k=(x-x_0)c_4^k, \tag{32}$$

$$c_6^k=(y-y_0)c_4^k, \tag{33}$$

$$\mathbf{P}=(u_0,u_x,u_y,v_0,v_x,v_y)^T, \tag{34}$$

$$\mathbf{P}^{k+1}=\mathbf{P}^k+\delta\mathbf{P}^k. \tag{35}$$

Practical implementation of Eqs. (12) and (25) requires the calculation of intensity values $I_1(\mathbf{r})$ and $I_2(\mathbf{r})$, as well as spatial gradients $\nabla I_1(\mathbf{r})$ and $\nabla I_2(\mathbf{r})$. In this paper, a bicubic spline interpolation algorithm is used to ensure the continuity and smoothness of the intensities and its first-order spatial derivatives. Initial guess of displacement and deformation gradient used in Eq. (25) is given by:

$$\mathbf{P}^0=(u_0,0,0,v_0,0,0)^T, \tag{36}$$

where u_0 and v_0 are determined using Eq. (12). Equations (25)–(35) are then implemented repeatedly until displacement and deformation gradient converge. Strains are then calculated under small deformation assumption:

$$\varepsilon_{xx}=u_x, \tag{37}$$

$$\varepsilon_{yy}=v_y, \tag{38}$$

$$\gamma_{xy}=u_y+v_x. \tag{39}$$

Previous DISC algorithms are based on the maximization of correlation coefficient through Newton's iteration (e.g., Ref. 10). This inevitably requires the calculation of second-order spatial derivatives of the two images, which increases computation complexity. One way to avoid high-order derivative calculation is to make approximations and drop high-order terms (e.g., Ref. 4). In this paper, a rigorous derivation is carried out that yields an algorithm that only requires the calculation of first-order spatial derivatives.

3 Verification of DISC Code Using Simulated Images

Computer simulated images can provide well-controlled image features and deformation information and are therefore used in this study to verify the DISC code as well as to study the impact of speckle size on the accuracy.

3.1 *Generation of Simulated Images*

Speckle patterns on the CCD target before and after deformation are assumed to be the sum of individual Gaussian speckles:

$$I_1(\mathbf{r})=\sum_{k=1}^{S} I_0\exp\left(-\frac{|\mathbf{r}-\mathbf{r}_k|^2}{a^2}\right), \tag{40}$$

$$I_2(\mathbf{r})=\sum_{k=1}^{S} I_0\exp\left(-\frac{|\mathbf{r}-\mathbf{U}(\mathbf{r})-\mathbf{r}_k|^2}{a^2}\right), \tag{41}$$

where S is the total number of speckles, a is speckle size, $\mathbf{r}_k=(x_k,y_k)^T$ are positions of each speckle with a random distribution, I_0 is the peak intensity of each speckle, $\mathbf{U}(\mathbf{r})$ is the displacement field calculated for given displacement and deformation gradient values:

$$\mathbf{U}(\mathbf{r})=\mathbf{U}_0+\nabla\mathbf{U}_0\mathbf{r}=\begin{pmatrix}u_0+u_x x+u_y y\\ v_0+v_x x+v_y y\end{pmatrix}. \tag{42}$$

These speckle patterns are then captured by the CCD target into discrete pixels, yielding:

$$I_1[i,j]=\sum_{k=1}^{S}\int_{i\cdot dx}^{i\cdot dx+\alpha\cdot dx}\int_{j\cdot dy}^{j\cdot dy+\beta\cdot dy} I_0\times\exp\left[-\frac{(x-x_k)^2+(y-y_k)^2}{a^2}\right]dx\,dy, \tag{43}$$

$$I_2[i,j]=\sum_{k=1}^{S}\int_{i\cdot dx}^{i\cdot dx+\alpha\cdot dx}\int_{j\cdot dy}^{j\cdot dy+\beta\cdot dy} I_0\times\exp\left[-\frac{(x-u_0-u_x x-u_y y-x_k)^2+(y-v_0-v_x x-v_y y-y_k)^2}{a^2}\right]\times dx\,dy, \tag{44}$$

where dx and dy are the pixel size, and α and β are duty cycles. In this study, dx, dy, α, and β are set to 1 for simplicity.

Equations (43) and (44) can be integrated analytically, yielding:

$$I_1[i,j]=\frac{1}{4}\pi a^2 I_0\sum_{k=1}^{S}\left[\mathrm{erf}\left(\frac{i-x_k}{a}\right)-\mathrm{erf}\left(\frac{i+1-x_k}{a}\right)\right]\times\left[\mathrm{erf}\left(\frac{j-y_k}{a}\right)-\mathrm{erf}\left(\frac{j+1-y_k}{a}\right)\right], \tag{45}$$

$$I_2[i,j]=\frac{1}{4}\pi a^2 I_0 J\sum_{k=1}^{S}\left[\mathrm{erf}\left(\frac{\xi_1-\xi_{0,k}}{a}\right)-\mathrm{erf}\left(\frac{\xi_2-\xi_{0,k}}{a}\right)\right]\times\left[\mathrm{erf}\left(\frac{\eta_1-\eta_{0,k}}{a}\right)-\mathrm{erf}\left(\frac{\eta_2-\eta_{0,k}}{a}\right)\right], \tag{46}$$

where

$$\xi_1=(1-u_x)i-u_y j, \tag{47}$$

$$\xi_2=(1-u_x)(i+1)-u_y(j+1), \tag{48}$$

$$\xi_{0,k}=x_k+u_0, \tag{49}$$

$$\eta_1=-v_x i+(1-v_y)j, \tag{50}$$

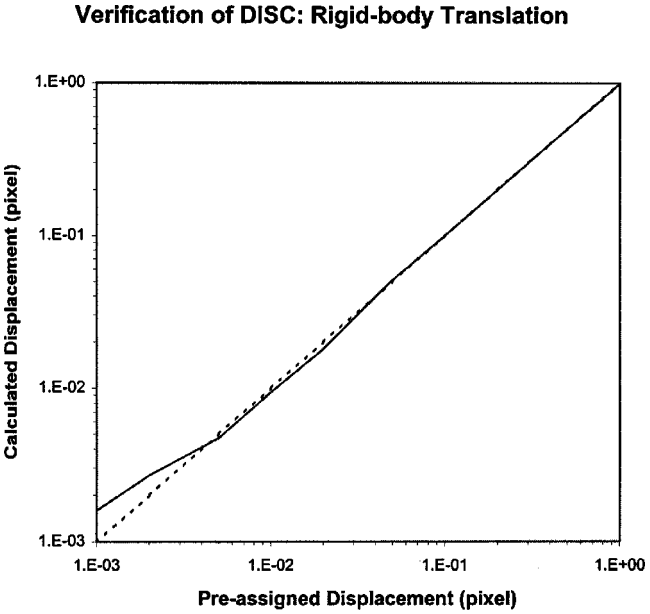

Fig. 2 Verification of DISC with rigid-body translation. The speckle image pairs are generated with $a=4$, SNR=20 dB, $S=100$, and $u_0=0.001\sim1$ pixel. The dashed line represents a perfect correspondence between calculated values and preassigned values.

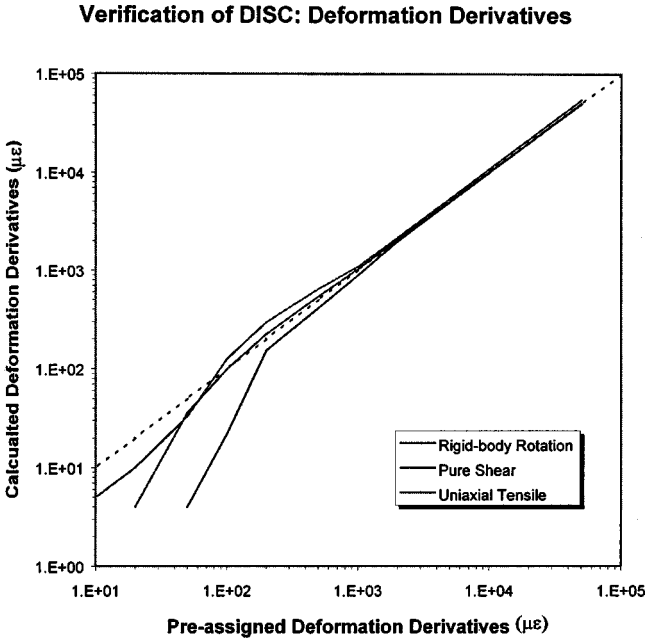

Fig. 3 Verification of DISC with rigid-body rotation, pure shear and uniaxial tensile. The speckle image pairs are generated with $a=4$, SNR=20 dB, $S=100$, and $\varepsilon=10\ \mu\varepsilon$ to 100,000 $\mu\varepsilon$. The dashed line represents a perfect correspondence between calculated values and preassigned values.

$$\eta_2=-v_x(i+1)+(1-v_y)(j+1), \tag{51}$$

$$\eta_{0,k}=y_k+v_0, \tag{52}$$

$$J=\det\begin{vmatrix}1-u_x & -u_y\\ -v_x & 1-v_y\end{vmatrix}. \tag{53}$$

Random noises with a given signal to noise ratio (SNR) are then added. Finally, these discrete values are digitized (8-bit) into two digital images.

3.2 *Verification of DISC Code Using Simulated Images*

Speckle images generated through Eqs. (45) and (46) are used to verify the DISC code, as well as to study the effect of speckle size on the accuracy of the DISC algorithm. Four typical deformation configurations are used to generate speckle image pairs before and after deformation: (1) rigid body translation with $\mathbf{U}(\mathbf{r})=(u_0,0)^T$, (2) rigid body rotation with $\mathbf{U}(\mathbf{r})=(\varepsilon\cdot y, -\varepsilon\cdot x)^T$, (3) uniaxial tensile with $\mathbf{U}(\mathbf{r})=(\varepsilon\cdot x, 0)^T$, and (4) pure shear with $\mathbf{U}(\mathbf{r})=(\varepsilon\cdot y, \varepsilon\cdot x)^T$. Other parameters such as S, SNR, and a are also assigned with typical values. Equation (5) is used to determine the integer-pixel displacement; subpixel displacement is then estimated using Eq. (12); this estimation is subsequently used as an initial guess for Eq. (25). Iteration of Eq. (25) gives the final displacement and deformation derivative values. A comparison of these calculated values with the preassigned values reveals the validity of the DISC code. The impact of speckle size on the accuracy of DISC is also studied by varying a.

3.3 *Results and Discussions*

Figures 2 and 3 show typical results for those four deformation configurations. The speckle image pairs are generated with $a=4$, SNR=20 dB, and $S=100$, and a preassigned rigid-body translation ($u_0=0.001\sim1$pixel), or preassigned deformation derivatives ($\varepsilon=10\ \mu\varepsilon\sim100{,}000\ \mu\varepsilon$). The dashed lines in these two figures represent a perfect correspondence between calculated values and preassigned values used in the simulator. As shown in these figures, the solid lines diverge from the dashed lines when the preassigned rigid-body translation is less than 0.005 pixel or the deformation derivatives are less than 1000 $\mu\varepsilon$. This indicates that DISC is capable of measuring subpixel displacement greater than 0.005 pixel and deformation derivatives greater than 1000 $\mu\varepsilon$. Different S, SNR, and a values show similar behavior.

Matrix $\mathbf{C}$ and vector $\mathbf{d}$ in Eq. (25) contain first-order spatial derivatives of two digital images. The accuracy of DISC therefore depends on the values of these spatial derivatives, i.e., the contrast features of the two images. Two important parameters contribute to the image contrast and thus to the accuracy of DISC: (1) noise and (2) speckle size.

3.3.1 *Noise*

Images acquired through CCDs may be contaminated by a variety of noise sources, such as photon noise, thermal noise, readout noise and shot noise. These noises can be characterized through a signal to noise ratio. Larger noises will lead to larger errors in the calculation of spatial derivatives and to worse accuracy. Noises can be alleviated through the use of high-performance hardware such as a cooled CCD, as well as frame averaging during image acquisition. A larger subimage Ω will also compensate the impact of noise despite its being more computationally de-

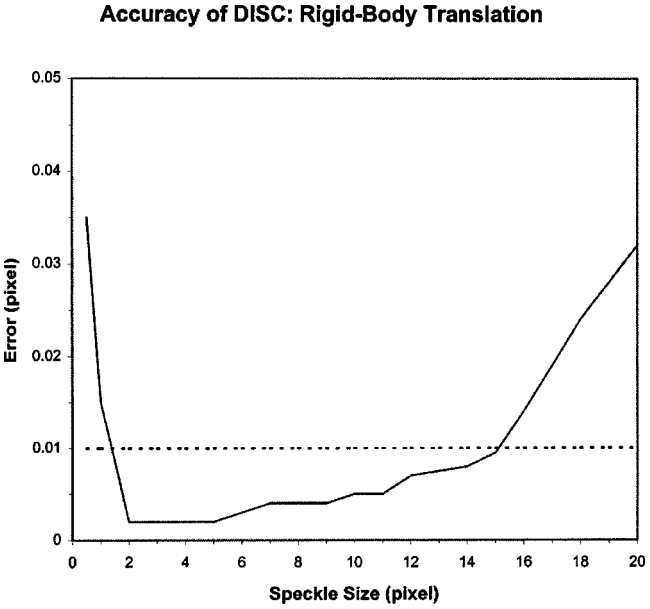

Fig. 4 Accuracy of DISC under rigid-body translation. The speckle image pairs are generated with SNR=20 dB, $S=100$, and $u_0=0.5$ pixel.

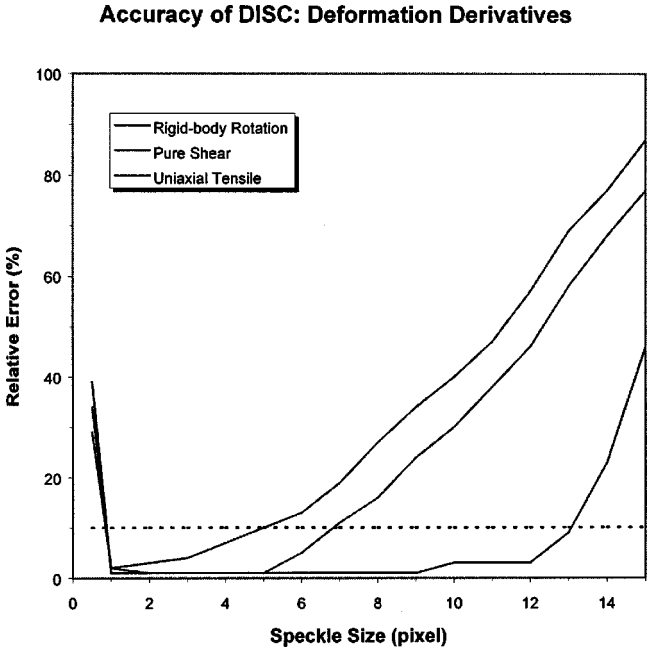

Fig. 5 Accuracy of DISC under rigid-body rotation, pure shear and uniaxial tensile. The speckle image pairs are generated with SNR=20 dB, $S=100$, and $\varepsilon=5000\ \mu\varepsilon$.

manding and will spatially average out deformation information.

3.3.2 *Speckle size*

The impact of speckle size on the accuracy of DISC is studied using simulated images. A typical result on the impact of speckle size on the accuracy of subpixel displacement calculation is shown in Fig. 4, with SNR=20 dB, $S=100$, and $u_0=0.5$ pixel. As we can see, there exists an optimal speckle size range for optimal accuracy. For this particular case, the optimal speckle size lies within 2 to 5 pixels. Similar results are obtained when varying SNR and S. The underlying explanation of this phenomenon is the accuracy of spatial-derivative calculation. Since the Nyquist frequency for the CCD target is 1, when speckle size is smaller than $\sim$2 pixels, undersampling occurs. Because of this undersampling, the calculated spatial derivatives cannot represent the true values on the specimen surface and thus lead to worse accuracy. In contrast, when the speckle size is too big, oversampling occurs. For a subimage with a fixed size, the number of speckles contained in the subimage is too small. Therefore, the subimage becomes too smooth and does not have enough spatial features to resolve the deformation data accurately. This can also explain the impact of speckle size on the accuracy of deformation gradient calculation for rigid-body rotation, uniaxial tensile and pure shear, as shown in Fig. 5, with SNR=20 dB, $S=100$, and $\varepsilon=5000\,\mu\varepsilon$. As we can see, there also exists an optimal speckle size range, 2 to 5 pixels. Similar results are obtained by varying SNR and S. It is coincidental that the empirical conclusion drawn by Bruck et al.[10] also falls in this range.

4 Calibration of DISC

After being verified through simulated images, DISC is then calibrated for rigid-body translation and rotation. The test speckle pattern is generated through spraying white paint onto a black surface. The sample is attached to a manual five-axis stage with a translation accuracy of 2 μm and a rotation accuracy of 0.01 rad. Images of the speckle pattern are captured through a microscope with a CCD camera and then digitized by a frame grabber with an 8 bit resolution. Cross-correlation of a reference image and a second image with a given rigid-body translation or rotation yields the deformation field of the sample, which is shown in Fig. 6. Calibration results clearly indicate the accuracy of the DISC code is below 0.01 pixel for rigid body translation and 500 $\mu\varepsilon$ for rigid body rotation. Using the same set of images under rigid body rotation, this calibration result has also matched the result from another algorithm developed at[11] NIST.

5 Applications of DISC

This paper also demonstrates the capability of DISC in thermomechanical diagnostics of electronic packaging, where thermomechanical deformation of the solder bumps has a great impact on packaging reliability. The sample under study is a FLIP-CHIP package (supplied by Motorola), which is cross-sectioned to expose a row of the solder bumps. A hot plate is used to control the sample temperature from room temperature to 100°C. The images of solder joints are captured through a microscope with a CCD camera and then digitized by a frame grabber with an 8 bit resolution. Cross correlation of the two images at different temperatures (25 and 100°C) yields thermomechanical deformation field of the solder joint, which is shown in Figs. 7(a) and 7(b). A detailed description of the application of DISC to thermomechanical diagnostics of electronic packaging can be found in another paper by the authors.[12]

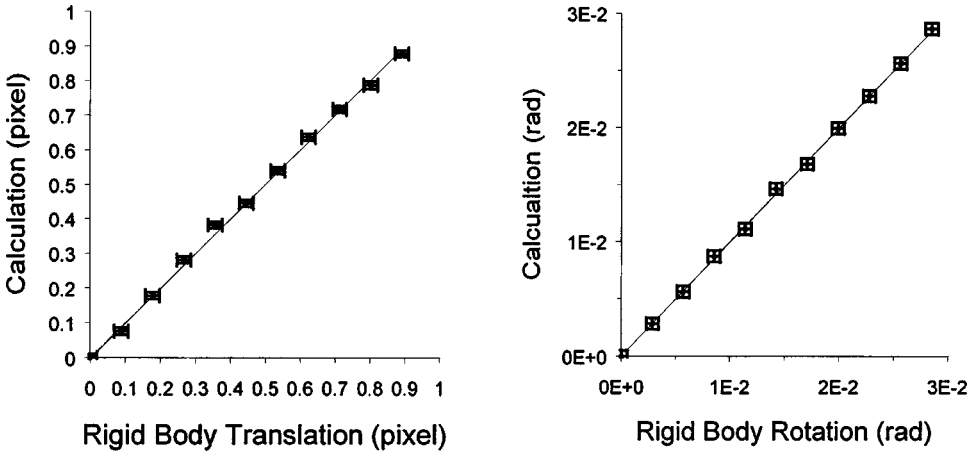

Fig. 6 Calibration of DISC under rigid-body translation and rigid-body rotation. The horizontal axes are preassigned rigid-body deformation, while the vertical axes are the results using the DISC code. The straight lines represent a perfect correspondence between calculated values and preassigned values.

6 Conclusions

In this paper, an iterative, spatial-gradient-based algorithm was developed, which requires the calculation of only first-order spatial derivatives of the images and thus reduces computation complexity. Simulated images with known deformation fields were then used to verify this algorithm, as well as to study the impact of speckle size on the accuracy. Based on these simulations, DISC is capable of measuring subpixel displacement greater than 0.005 pixel and deformation derivatives greater than 1000 $\mu\varepsilon$. In addition, an accuracy of 0.01 pixel for displacement and 10% for deformation derivatives greater than 1000 $\mu\varepsilon$ is indeed achievable. Simulations also suggest an optimal speckle size of 2 to 5 pixels for optimal accuracy. Calibration of the algorithm under rigid body translation and rotation yields an accuracy of 0.01 pixel for rigid body translation and 500 $\mu\varepsilon$ for rigid body rotation. DISC is also demonstrated to be a powerful metrology tool for thermomechanical diagnostics of electronic packaging.

Acknowledgments

The authors were supported by the Semiconductor Research Corporation through contracts PJ-357 and PJ-754. The authors thank Dr. Yifan Guo at Motorola for proving the FLIP-CHIP sample.

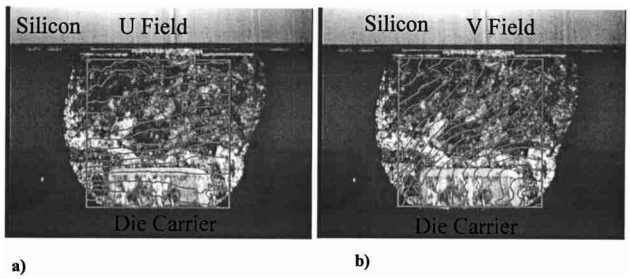

Fig. 7 In-plane thermomechanical deformations of a typical solder joint for the (a) *u* and (b) *v* deformation contours, with a spatial resolution of 0.25 μm/pixel and a deformation increment of 0.2 pixels.

References

1. D. J. Chen and F. P. Chiang, ''Computer-aided speckle interferometry using spectral amplitude fringes,'' *Appl. Opt.* **32**, 225–236 (1993).
2. W. H. Peters and W. F. Ranson, ''Digital imaging techniques in experimental stress analysis,'' *Opt. Eng.* **21**, 427–431 (1982).
3. P. C. MeKeighan, S. B. Seida, E. A. Franke, and D. L. Davidson, ''BISMAP: a non-contact displacement measurement system,'' in *Nontraditional Methods of Sensing Stress, Strain, and Damage in Materials and Structures*, ASTM 1318, G. F. Lucas and D. A. Stubbs, Eds., pp. 101–137, American Society for Testing and Materials, Philadelphia (1997).
4. G. Vendroux and W. G. Knauss, ''Submicron deformation field measurements: Parts 2. Improved digital image correlation,'' *Exp. Mech.* **38**, 86–92 (1998).
5. P. Buchhave, ''Particle image velocimetry: Status and trends,'' *Exp. Therm. Fluid Sci.* **5**, 586–604 (1992).
6. K. D. Hinsch, ''3-dimensional particle velocimetry,'' *Meas. Sci. Technol.* **6**, 742–753 (1995).
7. M. W. Collins, ''Holographic techniques for whole-field thermal and fluid measurements,'' *Aeronaut. J.* **95**, 313–323 (1991).
8. R. Erf, *Speckle Metrology*, p. 2, Academic Press, New York (1978).
9. C. Q. Davis and D. M. Freeman, ''Statistics of subpixel registration algorithms based on spatiotemporal gradients or block matching'' *Opt. Eng.* **37**, 1290–1298 (1998).
10. H. A. Bruck, S. R. McNeill, M. A. Sutton, and W. H. Peters, ''Digital image correlation using Newton-Raphson method of partial differential correction,'' *Exp. Mech.* **29**, 261–267 (1989).
11. D. T. Read, NIST, Private Correspondence (2000).
12. P. Zhou and K. E. Goodson, ''Thermomechanical diagnostics of BGA packages using digital image/speckle correlation (DISC),'' in *Proc. of 7th Intersociety Conference on Thermal and Thermochemical Phenomena in Electronic Systems (ITherm 2000)*, Vol. 2, pp. 240–245 Las Vegas, NV (2000).

Peng Zhou received his BS in 1995 and his MS in 1997 from the Department of Mechanical Engineering, the University of Science and Technology of China, where he was also awarded the Elite Experimental Science Prize in 1994, the Outstanding Undergraduate Student Prize in 1995, and the Guo Moruo Prize in 1997. His PhD research is focused on thermal and thermomechanical diagnostics and characterization of electronic packaging and multilevel interconnect systems.

Kenneth E. Goodson joined Stanford University in 1994, where he is an associate professor with the Mechanical Engineering Department. He received his BS in 1989, his MS in 1991, and his PhD in 1993 in mechanical engineering from the Massachusetts Institute of Technology, as well as a BS in 1989 and the Louis Sudler Prize in Humanities. Goodson was a visiting scientist at Daimler-Benz AG, Germany, where for sixteen months during 1993 and 1994 he was with the Materials Research Group working on the thermal design of power circuits for vehicles. His research has been recognized through the Office of Naval Young Investigator Award (Electronics Division, 1996–1999), the National Science Foundation CAREER Award (1996–2000), and the Best Student Paper Award at the 1992 IEEE Electron Devices Meeting. He advises a Daimler-Benz Circle Member Group Research and a Texas Instruments FMA Program. In spring 1996, he was a JSPS visiting professor at the Tokyo Institute of Technology.